PHYSICAL REVIEW B **96**, 024503 (2017)

Proximity-induced superconductivity in all-silicon superconductor /normal-metal junctions

F. Chiodi,[1,*] J.-E. Duvauchelle,[2] C. Marcenat,[2,3] D. Débarre,[1] and F. Lefloch[2]

[1]*Centre de Nanosciences et de Nanotechnologies, CNRS, Université Paris-Sud, Université Paris-Saclay, C2N Orsay, 91405 Orsay Cedex, France*

[2]*Université Grenoble Alpes, CEA-INAC-PHELIQS, F-38000 Grenoble, France*

[3]*Université Grenoble Alpes, Institut Néel, F-38000 Grenoble, France*

(Received 8 November 2016; revised manuscript received 28 April 2017; published 6 July 2017)

We have realized laser-doped all-silicon superconducting (S)/normal metal (N) bilayers of tunable thickness and dopant concentration. We observed a strong reduction of the bilayers' critical temperature when increasing the normal metal thickness, a signature of the highly transparent S/N interface associated to the epitaxial sharp laser doping profile. We extracted the interface resistance by fitting with the linearized Usadel equations, demonstrating a reduction of 1 order of magnitude from previous superconductor/doped Si interfaces. In this well-controlled crystalline system we exploited the low-resistance S/N interfaces to elaborate all-silicon lateral SNS junctions with long-range proximity effect. Their dc transport properties, such as the critical and retrapping currents, could be well understood in the diffusive regime. Furthermore, this work led to the estimation of important parameters in ultradoped superconducting Si, such as the Fermi velocity, the coherence length, or the electron-phonon coupling constant, fundamental to conceive all-silicon superconducting electronics.

DOI: 10.1103/PhysRevB.96.024503

I. INTRODUCTION

Quantum information is one of the main challenges in the search of faster, more efficient data treatment. In this frame, spin qubits made of isotopically purified silicon have recently emerged as one of the most promising technologies [1,2]. Indeed, silicon is an extremely well known material, where chemical purification, crystal growth, and defect control have been developed to a high extent. Similarly, micro- and nanofabrication clean room processes have been optimized for decades, allowing the realization of scalable devices. Finally, thanks to a low spin-orbit coupling and to the presence of stable isotopes without nuclear magnetic moment, it is possible to obtain inimitable electron and nuclear spin coherence times [1,2]. Silicon thus appears as a choice material to realize coherent quantum circuits, even more so when coupled to superconductivity, whose robustness and absence of dissipation were proven to be a great asset in the realization of the most advanced structures for quantum information [3,4]. Superconducting silicon offers a perfect solution to combine on the same chip the advantages of Si and superconductivity [5]. Obtained by laser doping, superconducting silicon layers can be epitaxied over a silicon substrate, form crystalline superconductor/doped Si interfaces without Schottky barriers (thanks to the comparable density of states), and ensure ohmic contacts with metals [6]. First studies have explored the superconductivity in Si:B and detailed its dependence on the doping parameters [6,7], and recently superconducting silicon SS'S Dayem Superconducting Quantum Interference Devices (SQUIDs) [8] have been realized with standard clean room processes. In this paper we demonstrate superconductor (S)/normal metal (N)/superconductor (S) junctions, fabricated entirely from laser-doped silicon SN bilayers. The bilayer and junction behavior could be modeled in the limit of diffusive superconductivity. The well-controlled technology, together with the demonstration of transparent interfaces between superconductor and silicon layers, constitutes an important step towards an all-silicon superconducting electronics.

II. LASER DOPING AND SAMPLE FABRICATION

The adopted doping technique, gas immersion laser doping (GILD), allows the realization of boxlike homogeneous boron-doped layers of varied active concentration (6×10^{18} cm^{-3} – 6×10^{21} cm^{-3}) and thickness (5–300 nm), with sharp, epitaxial Si/Si:B interfaces [9–11]. The doping takes place in a UHV chamber (10^{-9} mbar), where a puff of the precursor gas BCl_3 is injected onto the Si sample surface, saturating the chemisorption sites [12]. The substrate is then melted by a pulsed excimer XeCl laser of pulse duration 25 ns. The boron diffuses into the liquid silicon and is incorporated substitutionally: a Si:B crystal is epitaxied on the underlying silicon (Fig. 1). Because of the short pulse duration and the high recrystallization speed, boron concentrations larger than the solubility limit ($\sim 1 \times 10^{20}$ cm^{-3} [13]) and as high as 11 at. % (6×10^{21} cm^{-3}) can be obtained without the formation of B aggregates [14]. The good control over the structural properties is reflected in the electronic properties, as homogeneous superconducting layers can be realized with superconducting critical temperatures up to 0.7 K [7,15,16]. GILD thus allows us to fabricate thin layers with nanometric thickness control, a dopant concentration spanning a wide range, from the semiconducting to the metallic and superconducting limits, with a finely tuned superconducting T_c solely controlled by the boron dose.

III. SN BILAYERS

Laser-doped SN bilayers were fabricated from n-type Si wafers of resistivity 45 Ω cm. The SN bilayers consist in the superposition of a superconducting layer on top of a normal

*francesca.chiodi@u-psud.fr

 ©2017 American Physical Society

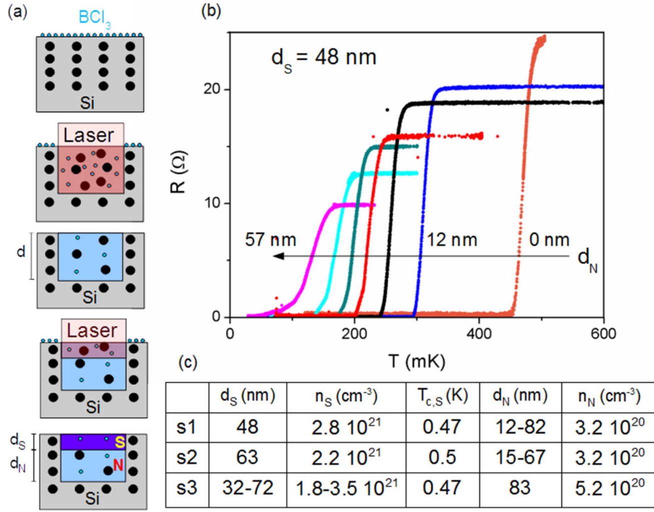

	d_S (nm)	n_S (cm^{-3})	$T_{c,S}$ (K)	d_N (nm)	n_N (cm^{-3})
s1	48	2.8 10^{21}	0.47	12-82	3.2 10^{20}
s2	63	2.2 10^{21}	0.5	15-67	3.2 10^{20}
s3	32-72	1.8-3.5 10^{21}	0.47	83	5.2 10^{20}

FIG. 1. (a) Bilayer fabrication: chemisorbtion of the precursor gas; laser melting of the substrate and dopant diffusion in the liquid phase; solidification and epitaxy of a normal metal Si:B crystal over the Si substrate; chemisorbtion and laser melting of a thin Si:B layer; epitaxy of a superconducting Si:B layer over the normal metal Si:B layer. (b) Resistive transitions $R(T)$ of SN bilayers (s1) with $d_N = 0,12,17,26,32,42,57$ nm. (c) Characteristics of the three bilayers series realized: thickness d_S, dopant concentration n_S, and critical temperature $T_{c,s}$ of the superconducting layer, thickness d_N, and dopant concentration n_N of the normal layer.

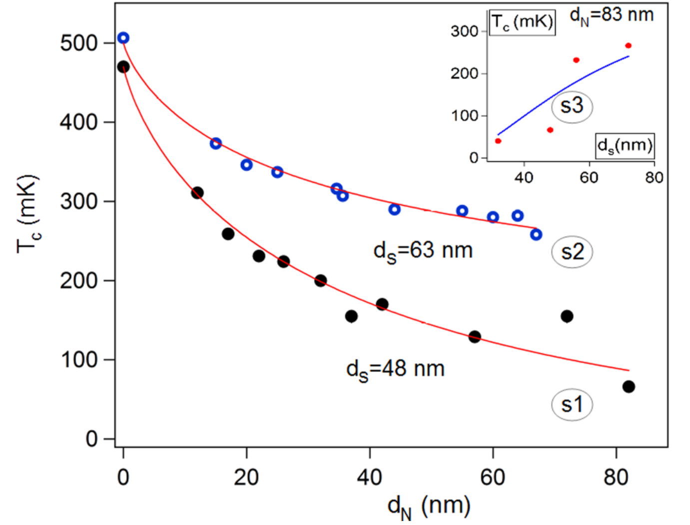

FIG. 2. Critical temperature T_c as a function of the normal layer thickness d_N for series s1 (dots) and s2 (circles). The lines are fits from Eq. (1) with $T_{c,S} = 0.47$ K and $b = 0.486$ for s1, $T_{c,S} = 0.5$ K and $b = 0.52$ for s2. (Inset) Critical temperature T_c as a function of the superconducting layer thickness d_S for series s3 (dots), fitted with Eq. (1) (line). This fit is less accurate than that of $T_c(d_N)$ due to the fact that we adopted an average $b = 0.6$ for s3 series. The b value actually ranges from 0.53 to 0.66, as the dopant concentration is varied in s3 in accordance to d_S to ensure a constant $T_{c,S}$.

(nonsuperconducting) layer. We started the fabrication by doping a normal layer of thickness d and dopant concentration n_N. We then reduced the laser energy and doped a thinner layer above the superconducting threshold [Fig. 1(a)]. This results in an upper superconducting layer of thickness d_S with a critical temperature $T_{c,S}$, on top of a bottom normal layer of thickness $d_N = d - d_S$ with a fixed dopant concentration n_N. Ti (15 nm)/Au (200 nm) contacts were then evaporated after a surface buffered hydrofluoric acid deoxidization. We realized two series of samples with constant d_S and varying d_N, s1 and s2, and a third series of samples with constant d_N and varying d_S, s3 (see Table 1(c) for details). Each series also includes a single superconducting layer of thickness d_S for reference.

In all the series, the S and N layer thicknesses were chosen to be smaller than, or comparable to, the superconductor coherence length $\xi_S \approx 80$ nm [17]: $d_S = 32 - 72$ nm $\lesssim \xi_S$ and $d_N = 12 - 83$ nm $\lesssim \xi_S$.

IV. LARGE T_c MODULATION

Characteristic resistive transitions of the s1 series SN bilayers are shown in Fig. 1(b). The transitions are quite sharp, their width varying between 25 and 58 mK. We observe a drastic reduction of the bilayer T_c when the normal layer thickness increases. We detail the dependence of T_c vs d_N in Fig. 2, where we show two series of bilayers, s1 and s2, of different $d_S = 48$ and 63 nm. We observe a monotonic T_c decrease with d_N, followed by a saturation at large d_N. The T_c reduction, as high as 86%, is more marked in the series of samples with the thinner superconducting layer, where the Cooper pairs spend comparatively more time in the normal metal. We understand qualitatively the saturation as the Cooper pairs explore the normal layer on an average depth ξ_S: when $d_N > \xi_S$, the superconductivity is no longer sensitive to an increased thickness of the normal layer.

V. HIGH INTERFACE QUALITY

The strong influence of the normal layer over the superconducting one supports the expectation of a transparent S/N interface. Indeed, the T_c suppression with d_N is determined by the interface resistance between the superconducting and the metallic doped Si layer. We could thus demonstrate an unprecedented low SN contact resistance in laser-doped silicon bilayers, thus enabling a long-range proximity effect.

We modeled the variation of T_c with d_N (at fixed d_S) and with d_S (at fixed d_N) with the analytical solution of the linearized Usadel equations near T_c in the limit of good transparency ($\tau \gg k_B T_c$) [18,19]:

$$T_c = T_{c,S}\left[\frac{T_{c,S}}{1.14\,\Theta_D}\sqrt{1+\left(\frac{k_B\Theta_D}{\tau}\right)^2}\right]^{b\frac{d_N}{d_S}}, \qquad (1)$$

$$\tau = \frac{\hbar}{2\pi}\frac{v_{F,S}}{\rho_{\text{int}}}\frac{b\,d_N + d_S}{b\,d_N\,d_S} \qquad b = \frac{v_{F,N}}{v_{F,S}} = \left(\frac{n_N}{n_S}\right)^{1/3}. \qquad (2)$$

As most of the parameters involved in the model are well known, either from direct measurements or from the literature, the interface resistance can be estimated through the fitting parameter ρ_{int}, the dimensionless interface resistance per channel. The total interface resistance per unit area is then given by taking all the conduction channels into account:

$R_{\text{int}}A = h/2e^2\,(\lambda_{F,S}/2)^2\,\rho_{\text{int}}$. The other parameters in the model are:

$T_{c,S}$: critical temperature of the single superconducting layer, measured independently.

Θ_D: phonon energy scale in temperature units, estimated from literature at 450 K [20].

$b = v_{F,N}/v_{F,S}$: ratio of the Fermi velocities in the normal and superconducting layers. In the free electron model, $v_F \propto k_F = (3\pi^2 n_B)^{1/3}$, giving $b = (n_N/n_S)^{1/3}$. The carrier densities were independently determined with Hall measurements (Table in Fig. 1).

$v_{F,S}$: Fermi velocity in the superconductor. Estimated to $v_{F,S} \approx 2.5 \pm 1 \times 10^5$ m/s from independently measured Si:B parameters ($T_c = 470$ mK, resistivity $\rho \approx 110\,\mu\Omega\,$cm, concentration $n_S \approx 2.8 \times 10^{21}$ cm^{-3}, and critical field $B_{c2,S}(0) \approx 940$ G) [21].

It is worth mentioning that the concentration at the bottom of the doped layer decreases to zero over $d' \approx$ a few nanometers, that will therefore not be superconducting. The normal layer thickness d_N is thus slightly larger, and d_S slightly smaller, than the doped depths. The best fits were obtained with $d' = 8$ nm for all series, in agreement with [7,9]. The initial hypothesis that $\tau \gg k_B T_c$ is reasonably confirmed, with $\tau/k_B T_c = 3$–27 in the range studied.

We show in Fig. 2 the good agreement obtained with the experimental data when adjusting the parameter ρ_{int}. We find $\rho_{\text{int}} = 4.4$ and $R_{\text{int}}A = 8 \times 10^{-10}\,\Omega\,\text{cm}^2$ for s1 and $\rho_{\text{int}} = 10$ and $R_{\text{int}}A = 2 \times 10^{-9}\,\Omega\,\text{cm}^2$ for s2. Even though the determination of ρ_{int} is affected by the uncertainty of the other parameters, the main conclusion here is that the interface obtained is in both cases extremely transparent, with a resistance smaller by an order of magnitude when compared to experimental [22–24] or theoretical [25] determinations of silicon/metallic superconductor contact resistance.

VI. COHERENCE AND SUPERCONDUCTING INTERFERENCES

We now describe the transport measurements realized on the bilayers through two contacts deposited on top of the superconducting layer. When increasing the current, we observe a switching from the superconducting to the resistive state at a critical current $I_c \approx 100$–$200\,\mu$A, and a strong hysteresis when reducing the current, with a retrapping current $I_r \approx 10$–$50\,\mu$A. This hysteresis can be attributed to typical heating effects, which will be treated in more detail further in the paper.

Figure 3(a) shows the low-current part of a typical differential resistance curve $dV/dI(I)$. Resistance peaks are observed in the resistive state of all the measured bilayers; note that the peak height and position are highly reproducible. We have studied the voltage, temperature, and magnetic field dependence of these peaks to identify their origin.

Figure 3(b) shows the voltage of the first seven peaks for two bilayers with different d_N. For each d_N, the peaks are equally spaced in voltage (successive peaks thus having linearly increasing voltages), with $\Delta V = 3$–$17\,\mu$V in the temperature range studied, 40–250 mK. When decreasing d_N, we observe an increase of ΔV. For $d_{N,1} = 26$ nm and $d_{N,2} = 22$ nm

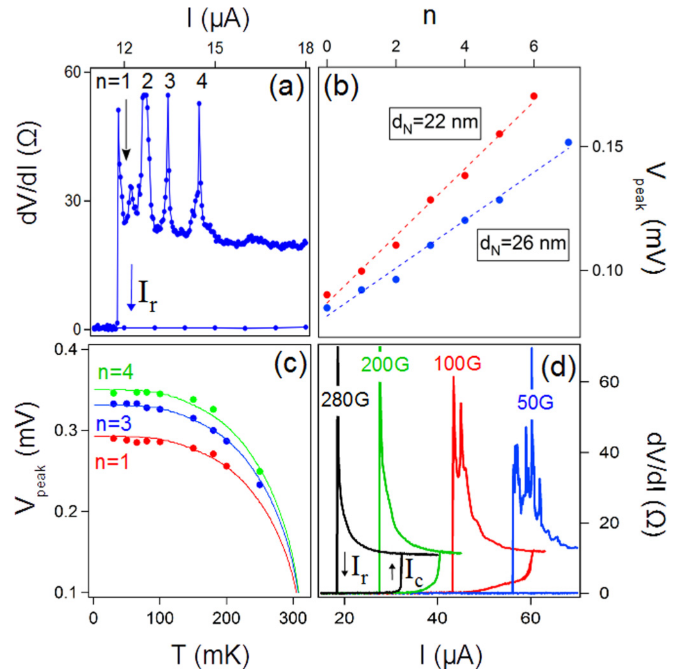

FIG. 3. (a) $d_S = 48$ nm, $d_N = 22$ nm: Differential resistance vs bias current at $T = 75$ mK. (b) $d_S = 48$ nm, $d_N = 22$ nm and 26 nm: Peak voltage in two bilayers of equal d_S and different d_N at $T = 75$ mK. We have arbitrarily attributed to the lower voltage peak observed the index $n = 0$. (c) $d_S = 63$ nm, $d_N = 34.5$ nm: Temperature dependence of three peak voltages compared to the BCS gap dependence [lines are traced for $V(T) = 6.1 \times \Delta(T)$, $6.9 \times \Delta(T)$, and $7.3 \times \Delta(T)$]. (d) $d_S = 57$ nm, $d_N = 23$ nm: Differential resistance curve as a function of the magnetic field at $T = 100$ mK.

we found a periodicity $\Delta V_1 = 9.7\,\mu$V and $\Delta V_2 = 13.6\,\mu$V, respectively. This would suggest a dependence $\Delta V \propto 1/d_N^2$. Indeed, $(d_{N,1}/d_{N,2})^2 = 1.4 = \Delta V_2/\Delta V_1$.

Figure 3(c) shows the temperature dependence of the peak voltage as compared to the temperature dependence of the BCS gap. The peaks disappear with temperature, and their dependence follows that of the BCS gap, demonstrating that the peaks are related to superconductivity. A magnetic field rapidly suppresses the peaks, which cannot be observed for $H > H_c/3$ [Fig. 3(d)]. They thus show a greater sensitivity to the magnetic field than the critical current, which is suppressed over the same magnetic field range by a factor 3.5 only.

These periodic peaks, due to superconducting interferences, may be explained in the framework of the Rowell-McMillan effect. In a bilayer formed by a superconductor and a normal metal with a good interface, an electron in the normal metal is reflected at the S/N interface into a coherent hole through an Andreev reflection. The hole can be specularly reflected at the N/substrate interface, and undergoes a second Andreev reflection at the superconductor interface. The interference between the first electron, and the electron resulting from two Andreev reflections and one specular reflection, can induce a series of equidistant peaks in the bilayer resistance. The expected peak periodicity in a ballistic system is $\Delta V = \hbar v_{F,N}/4d_N e$, as the charges cross 4 times the thickness of the normal layer in a ballistic time $\tau_b = 4d_N/v_{F,N}$. As in our case the normal layer is in the dirty limit, the diffusive

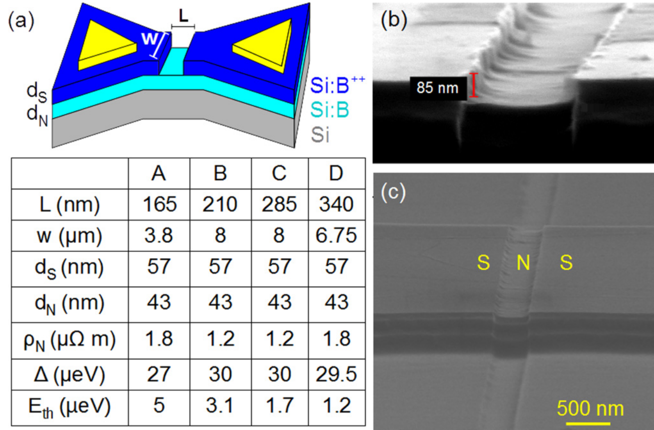

	A	B	C	D
L (nm)	165	210	285	340
w (μm)	3.8	8	8	6.75
d_S (nm)	57	57	57	57
d_N (nm)	43	43	43	43
ρ_N (μΩ m)	1.8	1.2	1.2	1.8
Δ (μeV)	27	30	30	29.5
E_{th} (μeV)	5	3.1	1.7	1.2

FIG. 4. (a) Sketch of the SNS junction geometry realized from a S/N (Si:B^{++}/Si:B) bilayer; (b, c) scanning electron microscopy images of the line etched in the upper superconducting layer and partially in the normal metal layer. (Table) Characteristics of the junctions shown in this paper: normal wire length L and width w, superconductor and normal metal thickness d_N and d_S, normal metal resistivity ρ_N, gap of the superconducting bilayer $\Delta = 1.78\, k_B T_c$, and Thouless energy $E_{Th} = \hbar D/L^2$, calculated from L, and the fitting value of the diffusion coefficient D.

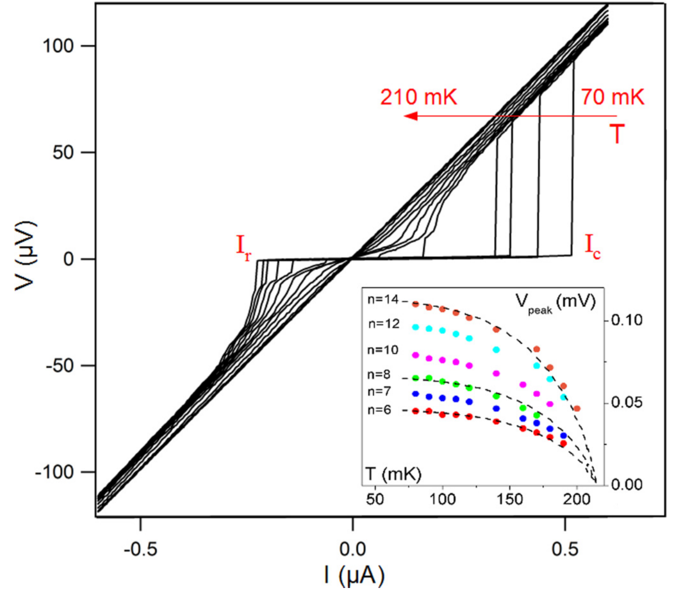

FIG. 5. $V(I)$ curves for junction A in the temperature range 70–210 K for increasing current. (Inset): Temperature dependence of the peak voltage compared to the BCS gap dependence [dotted lines for $1.4 \times \Delta(T)$, $2 \times \Delta(T)$, and $3.4 \times \Delta(T)$].

time is given by $\tau_D = (4d_N)^2/D$, leading to $\Delta V \propto 1/d_N^2$. The experimental values found are also compatible with this interpretation: for $d_N = 22$ nm we find $\Delta V = \hbar D/(4d_N)^2 e \approx 16\,\mu$V, for a diffusion coefficient $D \approx 2\,\mathrm{cm}^2\,\mathrm{s}$ calculated from $D = v_{F,N}\, l_e/3$, with $v_{F,N} = b \times v_{F,S} = 1.2 \times 10^5$ m/s and $l_e = 5$ nm. This estimate is in rough agreement with the observed periodicity of 13.6 μV.

We expect that these oscillations, rarely observed in metallic systems, are enhanced in our devices thanks to the sharp epitaxial interface between the Si substrate and the Si:B crystalline N layer where the specular reflection takes place, illustrating again the quality of the realized structures. It is also worth noting that the peaks are observed up to the seventh order of interference; this implies that the phase coherence length is not strongly limited by inelastic diffusion phenomena and extends at least to a few hundreds of nanometers.

VII. SNS JUNCTIONS

SNS junctions were realized from SN bilayers with $d_S = 57$ nm, $d_N = 58$ nm, $T_c = 200$ mK, and a normal layer concentration of $5.2 \times 10^{20}\,\mathrm{cm}^{-3}$. The device contacts and the wire width w : 3.8–8 μm were defined by reactive ion etching (RIE). Then, a thin line was drawn across the wire and the superconducting upper layer was etched by RIE, along with the first 15 nm of the normal layer, reducing d_N to 43 nm (Fig. 4; the depth was measured directly in samples B and C, and the same etching conditions were adopted for samples A and D). The overetch is performed to suppress completely the superconductor in the weak link, so that no superconducting bridges are left. The normal layer bridge length was set in the range L : 165–340 nm (junctions A,B,C,D), giving a Thouless energy $E_{Th} = 1.2$–$5\,\mu$eV $< \Delta \approx 30\,\mu$eV (Table, Fig. 4). As $\Delta \approx 10\, E_{Th}$, our junctions are in the intermediate regime between the long and the short junction limit [26].

The junctions presented here were fabricated in three runs, each run containing 2–3 junctions on the same laser-doped spot, junctions B and C belonging to the same run. We avoid quantitatively comparing junctions of different runs, even though the results are qualitatively reproducible for all the junctions, as fluctuation in the fabrication, such as in the overetch, can affect the junction properties.

The junction $V(I)$ curves (Fig. 5) show standard characteristics: a sharp jump when the junction switches to the resistive state at the critical current $I_c \approx 0.5$–$3\,\mu$A, and a hysteresis cycle when, reducing the bias current, the junction switches back to the superconducting state at the retrapping current $I_r < 1\,\mu$A. As in the bilayers, multiple plateaus appear in the normal region of the V-I curves (as equidistant peaks appear in the dV/dI curve), whose origin can be traced back to the bilayers. This is supported by the temperature dependence of the plateaus (Fig. 5 inset), which follows, as in the case of the bilayers, the dependence of $\Delta(T)$.

VIII. TEMPERATURE

Figure 6(a) displays the temperature dependence of the critical current in two junctions (B and C) of different lengths, $L = 210$ nm and $L = 285$ nm [Fig. 6(a)]. The critical current dependence on temperature has been fitted with the de Gennes expression for a dirty doped semiconductor weak link. This expression is valid in the linear limit for small induced pair correlations ($T \gtrsim T_c/2 \approx 100$ mK) [27]:

$$I_c(T) \propto \frac{1}{\xi_N} \left(\frac{\Delta(T)}{\cosh(L/2\xi_N)} \right)^2. \tag{3}$$

The coherence length in the normal wire, ξ_N, is dominated by the thermal coherence length and was calculated following

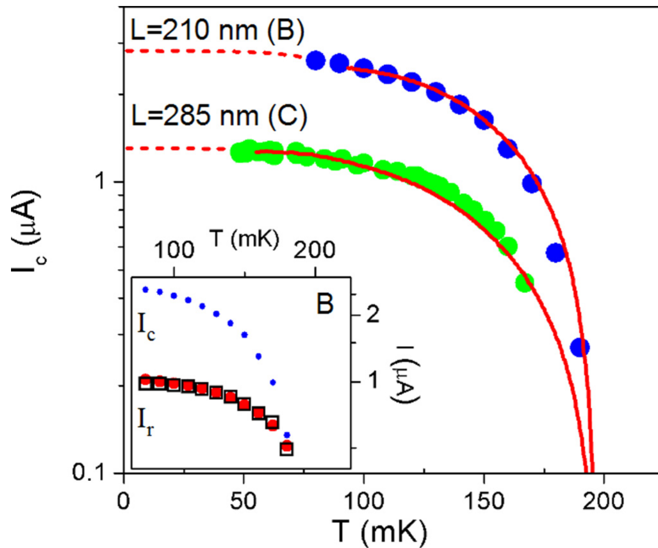

FIG. 6. $I_c(T)$ for junctions B and C. Lines: fits from Eq. (3). Dotted lines: zero-temperature limit. Inset: $I_c(T)$ and $I_r(T)$ for junction B. $I_r(T)$ fit (squares) assuming a heating-generated hysteresis.

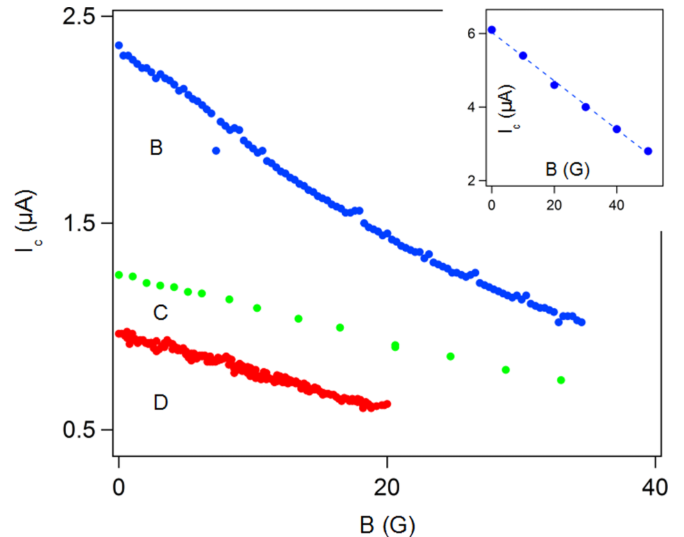

FIG. 7. I_c vs B at $T = 100$ mK for junctions B ($L \times w = 1.68\,\mu\text{m}^2$), C ($L \times w = 2.28\,\mu\text{m}^2$), and D ($L \times w = 2.3\,\mu\text{m}^2$). Inset: I_c vs B for a wide section of a SN bilayer (60 μm long and 160 μm wide), with $d_S = 57$ nm and $d_N = 58$ nm. The linear behavior follows $d(I_c)/dB = -0.066\,\mu$A/G.

[28,29]

$$\xi_N = \sqrt{\frac{\hbar^3\,\mu}{6\pi k_B T e m^*}}\,(3\pi^2 n_N/v)^{1/3}, \tag{4}$$

with the ratio of the conduction and DOS effective masses $m^* = m_c/m_{DOS}^2 = 0.34\,m_e$, $n_N = 5.2 \times 10^{20}$ cm^{-3}, the valley degeneracy for holes in Si $v = 1$, and the mobility $\mu = 55$ cm^2/V s, in reasonable agreement with the mobility estimated from the measured resistivity at low temperature, $\mu = 1/en_N\rho \approx 60$ cm^2/V s. The calculated coherence length in the normal weak link at $T_c = 197$ mK is $\xi_N(T_c) \approx 115$ nm; this value is larger than the coherence length in the superconductor ξ_S, as the mobility in the less-doped Si weak link is higher than in the more disordered superconducting Si.

Note that a reasonable agreement of the critical current temperature dependence could also be obtained with the models developed in Ref. [30], describing a SN-N-NS "sandwich" junction in the dirty limit with no potential barrier at the SN interface and rigid boundary conditions, or in Ref. [31], describing a SS'S/SNS junction in the dirty limit with small interface resistance ($\gamma_B = 0.1$) and L of the order of the coherence length.

Having described the general temperature dependence, we now concentrate on the low-temperature asymptotic value of the critical current. To do so, it is necessary to explicitly take into account the intermediate regime between the short and the long junction limit, solving the Usadel equations at low temperature. Indeed, while in a short junction the critical current is expected to saturate at low temperature at $e\,R_N\,I_c(0) = 2.08\,\Delta(0)$ [26], in the intermediate regime $e\,R_N\,I_c(0) = a\,\Delta(0)$. a decreases monotonically and smoothly when the ratio E_{Th}/Δ decreases towards the opposite limit, the long junction limit, where $\Delta \gg E_{Th}$ and $e\,R_N\,I_c(0) = 10.82\,E_{Th}$ [26]. We can thus extract the value of E_{Th} from a. For junction B, we find $a = 0.64$ and $E_{Th}/\Delta = 0.105$, while for junction C, we find $a = 0.42$ and $E_{Th}/\Delta = 0.057$. Assuming the same diffusion coefficient in both junctions, we confirm that $E_{Th,B}/E_{Th,C} = 1.84 = (L_C/L_B)^2$. Moreover, the diffusion coefficient deduced from E_{Th}, $D = 2.2$ cm^2/s, is in good agreement with our previous estimate ($D = 2$ cm^2/s). Such confirmation is important, as parameters such as l_e or v_F are not well known for the peculiar material that is ultradoped silicon but are of a fundamental importance to estimate the performances of superconducting silicon-based devices.

The inset of Fig. 6 shows the temperature dependence of the retrapping current I_r, compared to $I_c(T)$ in junction B. At low temperature, a hysteresis can be observed, as the switching current from the normal to the superconducting state I_r is smaller than the critical current I_c; at $T > 180$ mK, the hysteresis disappears as $I_c = I_r$. SNS junctions often present similar hysteresis at low temperature, due to the heating of the junction by the Joule power generated in the resistive state [32]. At low temperature, the phonon cooling power is limited and the injected heat cannot be instantly dissipated. The electronic temperature T_{el} is then larger than the phonon temperature T_{ph}, and the junction can switch back in the superconducting state only at $I_r = I_c(T_{el}) < I_c(T_{ph})$. Our observations confirm such heating effect: the hysteresis disappears at higher temperatures, and we can fit the retrapping current evolution by assuming a phonon cooling power $P = \Sigma\,V\,(T_{el}^5 - T_{ph}^5)$ with $\Sigma = 5.2 \times 10^7$ W/K^5 m^3. This value is in good agreement with the phonon cooling power measured for n-Si films of similar strong doping [33].

IX. MAGNETIC FIELD

We examined the behavior of both bilayers and junctions in a perpendicular magnetic field. Figure 7 shows the I_c vs H dependence of three junctions of different lengths. All show an overall linear dependence as the critical current decreases with the field in a range of a few tens of gauss. A wide section

of a SN bilayer (60 μm long and 160 μm wide) is also shown for comparison and presents a linear decrease of the critical current with the magnetic field over a comparable range. The superconductivity in the bilayer, and thus in the junctions' contact pads, is quickly suppressed by the magnetic field, reducing at the same time the junctions' critical current. This envelope dominates the junctions with the weakest I_c, while a rounded shape can be perceived in junction B. To explain the absence of the minima of the expected Fraunhofer pattern, that should be still visible despite the envelope, we estimated the importance of the self-field effects. Indeed, the width of the junctions studied (3.8–8 μm) is of the same order of magnitude as the Josephson length [34]:

$$\lambda_J = \sqrt{\frac{\hbar}{2e\mu_0(L + 2\lambda_L)J_c}}, \tag{5}$$

where $\lambda_L \approx 120$ nm is the London penetration length for the superconducting Si:B layer calculated from the previous estimations. For the three junctions shown, we have, respectively, $\lambda_J = 7.9\ \mu\text{m} \approx \text{w} = 8\ \mu\text{m}$ (junction B); $\lambda_J = 10\ \mu\text{m} \gtrsim \text{w} = 8\ \mu\text{m}$ (junction C); $\lambda_J = 10\ \mu\text{m} > \text{w} = 6.75\ \mu\text{m}$ (junction D). The self-field tends to induce a linear dependence of the $I_c(H)$ curve, but the amplitude of the effect is not sufficient to cancel the Fraunhofer minima completely [34]. We expect that a strong inhomogeneity of the current lines distribution may further contribute to the monotonic suppression observed.

X. CONCLUSIONS

We have realized all-silicon superconducting/normal metal bilayers of variable thickness and doping, which we have successfully modeled in the frame of diffusive metallic superconductors. We demonstrated a transparent S/N interface, an asset of the epitaxial sharp interface realized, with an interface resistance lower by an order of magnitude than metal/doped Si contact resistances. In this well-controlled, crystalline system, we also observed differential resistance peaks, equally spaced in voltage. These superconductivity-induced interferences, visible thanks to a long phase coherence length, are consistent with the Rowell-McMillan effect, but further investigation is necessary to confirm this hypothesis. Finally, we exploited the low-resistance S/N interfaces to realize all-silicon lateral SNS junctions from the SN bilayers. We observed a full proximity effect with a critical current of a few μA. The transport features, such as the I-V characteristic or the temperature dependence of the critical and retrapping current, could be well understood and modeled. Furthermore, this work led to the estimation of important parameters in ultradoped superconducting Si, such as the Fermi velocity, the coherence length, or the electron-phonon coupling constant, extremely useful to estimate the performance of future superconducting silicon-based devices.

ACKNOWLEDGMENTS

We are grateful to J. R. Coudevylle for help with the fabrication, and to H. Bouchiat, H. Cercellier, M. V. Feigel'man, S. Guéron, and T. Klein for fruitful discussions. We acknowledge the Réseau RENATECH, the FCS Triangle de la Physique ("DownTo40" project), the French National Research Agency (ANR-NanoQuartet, Grant No. NR12BS1000701), and the CEA Nanoscience Transverse Program for their financial support.

[1] K. Saeedi, S. Simmons, J. Z. Salvail, P. Dluhy, H. Riemann, N. V. Abrosimov, P. Becker, H.-J. Pohl, J. J. L. Morton, and M. L. W. Thewalt, Science **342**, 830 (2013).
[2] J. T. Muhonen, J. P. Dehollain, A. Laucht, F. E. Hudson, R. Kalra, T. Sekiguchi, K. M. Itoh, D. N. Jamieson, J. C. McCallum, A. S. Dzurak, and A. Morello, Nat. Nanotechnol. **9**, 986 (2014).
[3] T. Brecht, W. Pfaff, C. Wang, Y. Chu, L. Frunzio, M. H. Devoret, and R. J. Schoelkopf, npj Quantum Information **2**, 16002 (2016).
[4] M. H. Devoret and R. J. Schoelkopf, Science **339**, 1169 (2013).
[5] Y. Shim and C. Tahan, Nat. Commun. **5**, 4225 (2014).
[6] F. Chiodi, A. Grockowiak, J. E. Duvauchelle, F. Fossard, F. Lefloch, T. Klein, C. Marcenat, and D. Débarre., Appl. Surf. Sci. **302**, 209 (2014).
[7] A. Grockowiak, T. Klein, H. Cercellier, F. Levy-Bertrand, X. Blase, J. Kačmarčik, T. Kociniewski, F. Chiodi, D. Débarre, G. Prudon, C. Dubois, and C. Marcenat, Phys. Rev. B **88**, 064508 (2013).
[8] J. E. Duvauchelle, A. Francheteau, C. Marcenat, F. Chiodi, D. Débarre, K. Hasselbach, J. R. Kirtley, and F. Lefloch, Appl. Phys. Lett. **107**, 072601 (2015).
[9] A. Bhaduri, T. Kociniewski, F. Fossard, J. Boulmer, and D. Débarre, Appl. Surf. Sci. **258**, 9228 (2012).
[10] D. Cammilleri, F. Fossard, D. Débarre, C. Tran Manh, C. Dubois, E. Bustarret, C. Marcenat, P. Achatz, D. Bouchier, and J. Boulmer, Thin Solid Films **517**, 75 (2008).
[11] C. Marcenat, J. Kačmarčik, R. Piquerel, P. Achatz, G. Prudon, C. Dubois, B. Gautier, J. C. Dupuy, E. Bustarret, L. Ortega, T. Klein, J. Boulmer, T. Kociniewski, and D. Débarre, Phys. Rev. B **81**, 020501 (2010).
[12] J. Boulmer, C. Guedj, and D. Débarre, Thin Solid Films **294**, 137 (1997).
[13] A. J. Murrell, E. J. H. Collart, M. A. Foad, and D. Jennings, J. Vac. Sci. Technol. B **18**, 462 (2000).
[14] K. Hoummada, F. Dahlem, T. Kociniewski, J. Boulmer, C. Dubois, G. Prudon, E. Bustarret, H. Courtois, D. Débarre, and D. Mangelinck, Appl. Phys. Lett. **101**, 182602 (2012).
[15] F. Dahlem, T. Kociniewski, C. Marcenat, A. Grockowiak, L. M. A. Pascal, P. Achatz, J. Boulmer, D. Débarre, T. Klein, E. Bustarret, and H. Courtois, Phys. Rev. B **82**, 140505 (2010).
[16] A. Grockowiak, T. Klein, E. Bustarret, J. Kačmarčik, C. Dubois, G. Prudon, K. Hoummada, D. Mangelinck, T. Kociniewski, D. Débarre, J. Boulmer, and C. Marcenat, Supercond. Sci. Technol. **26**, 045009 (2013).
[17] A. Grockowiak, Ph.D. thesis, Institut Néel (CNRS) and Laboratoire de Transport Electronique Quantique et Supraconductivité, INAC, Commissariat à l'Energie Atomique, 2012.
[18] S. Guéron, Ph.D. thesis, Quantronics group, Commissariat l'Energie Atomique, Saclay 1997.
[19] Ya. V. Fominov and M. V. Feigel'man, Phys. Rev. B **63**, 094518 (2001).

[20] L. Boeri, J. Kortus, and O. K. Andersen, Phys. Rev. Lett. **93**, 237002 (2004).
[21] Y.-P. Shim and C. Tahan, IEEE J. Sel. Top. Quantum Electron. **21**, 9100209 (2015).
[22] B. Buonomo, R. Leoni, M. G. Castellano, F. Mattioli, and G. Torrioli, J. Appl. Phys. **94**, 7784 (2003).
[23] D. Quirion, F. Lefloch, and M. Sanquer, J. Low Temp. Phys. **120**, 361 (2000).
[24] R. C. Ruby and T. Van Duzer, IEEE Trans. Electron Devices **28**, 1394 (1981).
[25] C. Y. Chang, Y. K. Fang, and S. M. Sze, Solid-State Electron. **14**, 541 (1971).
[26] P. Dubos, H. Courtois, B. Pannetier, F. K. Wilhelm, A. D. Zaikin, and G. Schon, Phys. Rev. B **63**, 064502 (2001); Y.-P. Dubos, Ph.D. thesis, Centre de Recherches sur les Très Basses Températures , Grenoble, 2000.
[27] J. Seto and T. Van Duzer, Low Temp. Phys., LT-13 **3**, 328 (1974).
[28] W. M. van Huffelen, T. M. Klapwijk, D. R. Heslinga, M. J. de Boer, and N. van der Post, Phys. Rev. B **47**, 5170 (1993).
[29] A. Serfaty, J. Aponte, and M. Octavio, J. Low Temp. Phys. **63**, 23 (1986).
[30] A. A. Golubov, M. Yu. Kupriyanov, and V. F. Lukichev, Mikroelektronika **12**, 342 (1983) [Sov. Microelectronics **12**, 180 (1983)]; Iu. P. Baryshev, A. G. Vasil'Ev, A. A. Dmitriev, M. Iu. Kupriianov, and V. F. Lukichev, *Problems of Lithography in Microelectronics* (Izdatel'stvo Nauka, Moscow, 1987), p. 136.
[31] M. Yu. Kuprianov and V. F. Lukichev, Sov. Phys. JETP **67**, 1163 (1988).
[32] H. Courtois, M. Meschke, J. T. Peltonen, and J. P. Pekola, Phys. Rev. Lett. **101**, 067002 (2008).
[33] F. Giazotto, T. T. Heikkilá, A. Luukanen, A. M. Savin, and J. P. Pekola, Rev. Mod. Phys. **78**, 217 (2006).
[34] A. Barone and G. Paternó, *Physics and Applications of the Josephson Effect* (Wiley, New York, 1982).